

Structural defects in multiferroic BiMnO₃ studied by transmission electron microscopy and electron energy-loss spectroscopy

H. Yang, Z. H. Chi, L. D. Yao, W. Zhang, F. Y. Li, C. Q. Jin, and R. C. Yu^{a)}

Laboratory for Extreme Condition Physics, Beijing National Laboratory for Condensed Matter Physics, Institute of Physics, Chinese Academy of Sciences P.O. Box 603, Beijing 100080, People's Republic of China

(Received 8 December 2005; accepted 27 May 2006; published online 18 August 2006)

The multiferroic material BiMnO₃ synthesized under high pressure has been systematically studied by transmission electron microscopy and electron energy-loss spectroscopy, and some important structural defects are revealed in this multiferroic material. The frequently observed defects are characterized to be $\Sigma 3(1\bar{1}1)$ twin boundaries, Ruddlesden-Popper [Acta Crystallogr. **11**, 54 (1958)] antiphase boundaries, and $a_p\langle 001 \rangle_p$ superdislocations connected with a small segment of Ruddlesden-Popper defect. These defects are present initially in the as-synthesized sample. In addition, we find that ordered voids (oxygen vacancies) are easily introduced into the multiferroic BiMnO₃ by electron-beam irradiation. © 2006 American Institute of Physics.

[DOI: [10.1063/1.2245199](https://doi.org/10.1063/1.2245199)]

I. INTRODUCTION

Multiferroic materials, displaying simultaneously ferromagnetism and ferroelectricity, are currently attracting growing interests due to their intriguing physical phenomena and potential applications. However, multiferroic materials are rare in nature because the physical/structural/chemical conditions for a material to be simultaneously ferromagnetic and ferroelectric are generally difficult to be achieved.^{1,2} BiMnO₃ with a perovskite-type structure is one of the rare examples of multiferroics. It has been well proven that the perovskite-type BiMnO₃ becomes ferromagnetically ordered on cooling below ~ 105 K,³⁻⁷ and there is good reason to believe that ferromagnetism coexists with ferroelectricity.^{8,9} Although ferroelectricity is difficult to observe due to the low resistance of films and the lack of large high-quality bulk samples, experimental evidence for the possible occurrence of magnetoferroelectricity in BiMnO₃ has been reported by Moreira dos Santos *et al.*⁵ and Kimura *et al.*¹⁰ At room temperature, the perovskite-type BiMnO₃ forms a monoclinic superstructure with a space group $C2$ and the lattice parameters $a=9.53$ Å, $b=5.61$ Å, $c=9.85$ Å, and $\beta=110.67^\circ$.¹¹ A structural phase transformation from the monoclinic $C2$ to an orthorhombic $Pbnm$ has been observed at ~ 770 K,¹⁰ at which a ferroelectric phase transition likely occurs in terms of crystallography.

The final properties (especially for ferroelectricity) of a multiferroic largely depend on the concentration and types of defects in its structure. Taking ferroelectrics, for example, a Monte Carlo simulation study revealed that defects play a major role in determining the shapes of hysteresis curves.¹² The importance of defects in determining the final properties of a ferroelectric has also been underlined by large numbers of experimental studies. For example, investigations on lead zirconate titanate (PZT) ceramics have suggested that defects

such as oxygen vacancies interact strongly with domain boundaries and dominate the polarization properties.¹³ Therefore, structural defects studied whether in monoferroics or in multiferroics are becoming a subject of intense interest. For the important multiferroic BiMnO₃, however, no detailed defect analysis at atomic level has been carried out, and the types of defects possibly existing in it have not yet been known. In this paper, through careful investigation on a high-pressure synthesized sample of BiMnO₃ using transmission electron microscopy (TEM) and electron energy-loss spectroscopy (EELS) techniques, we reveal in this multiferroic material some important structural defects, including $\Sigma 3(1\bar{1}1)$ twin boundaries, Ruddlesden-Popper (RP) antiphase boundaries, and $a_p\langle 001 \rangle_p$ superdislocations formed under high temperature and high pressure, and voids (ordered oxygen vacancies) induced by electron-beam irradiation.

II. EXPERIMENT

Using Bi₂O₃ (Alfa Aesar 99.99%) and Mn₂O₃ (Alfa Aesar 98%) as starting materials, polycrystalline BiMnO₃ specimen was synthesized at 1173 K and 5 GPa for 30 min. Details of the sample preparation have been described in Ref. 14. Thin foils for TEM studies were prepared by crushing the bulk specimen in an agate mortar filled with alcohol, and then dispersing the fine fragments suspended in alcohol on a microgrid. A Tecnai F20 field-emission electron microscope installed at the Beijing Laboratory of Electron Microscopy, Beijing National Laboratory for Condensed Matter Physics was used for electron diffraction (ED), high-resolution transmission electron microscopy (HRTEM), and EELS experiments. All the TEM studies were carried out at an acceleration voltage of 200 keV.

^{a)}Author to whom correspondence should be addressed; electronic mail: rcyu@aphy.iphy.ac.cn

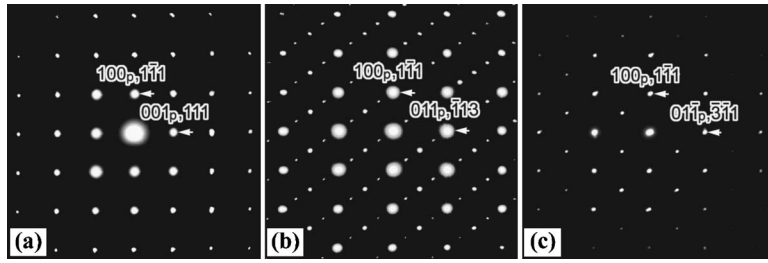


FIG. 1. Selected area ED patterns of BiMnO₃ along (a) [010]_p (or [101]_l), (b) [011]_p (or [110]_l), and (c) [011]_p (or [011]_l) zone axes, indicating a C2 monoclinic superstructure.

III. RESULTS AND DISCUSSION

A. Crystal structure identification by TEM

The high-pressure synthesized BiMnO₃ sample is first characterized structurally by TEM. At room temperature, the perovskite-type BiMnO₃ has been determined by powder neutron diffraction measurements to be a monoclinic modulated superstructure with space group C2.¹¹ This monoclinic superstructure is confirmed further by our resultant ED and HRTEM data. Figure 1 shows some zone-axis ED patterns, indicating that the crystal exhibits a four-fold periodicity along the [111]_p direction of the fundamental perovskite structure (hereinafter the subscript *p* stands for the fundamental perovskite-type structure). This modulated structure agrees well with the reported C2 superstructure.¹¹ All the patterns are indexed according to the perovskite structure as well as the C2 superstructure, clearly revealing the relation of the structures between fundamental perovskite and the C2 modulated phase. Figure 2 shows a HRTEM image taken along the [011]_p (or [110]_l) zone-axis direction. This image was obtained under a defocus value of ~ -65 nm. Image simulations based on the structure model proposed in Ref. 11 were carried out by varying defocus value from -60 to -70 nm and crystal thickness. A simulated image for a defocus value of -65 nm and a thickness of 15 nm, embedded in the image, appears to be in good agreement with the experimental one. In addition, no TEM evidence shows the existence of nonmodulated triclinic phase in our sample.

B. Intrinsic defects (twin boundaries, antiphase boundaries, and dislocations) formed under high temperature and high pressure

Twin boundaries, antiphase boundaries, and dislocations are the common defects observed in the high-pressure syn-

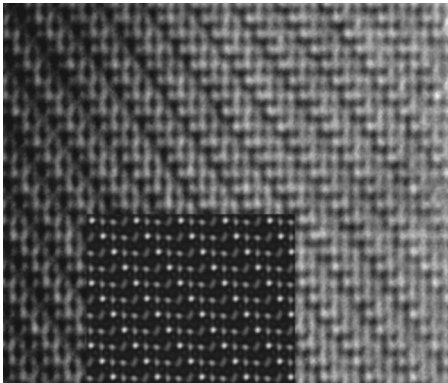


FIG. 2. HRTEM image of BiMnO₃ taken along the [011]_p (or [110]_l) zone-axis direction. A simulated image is superimposed onto the experimental image.

thesized BiMnO₃ sample. These defects are present in the sample from the beginning, unlike the products induced by electron-beam irradiation.

The typical twin boundary observed in the sample is the $\Sigma 3(1\bar{1}1)$ twin boundary. Figure 3(a) shows, as an example, a HRTEM image of this kind of twin boundary. The fast Fourier transform (FFT) patterns corresponding to the left and right grains are shown, respectively, in Figs. 3(b) and 3(c), and reveal clearly a twinning relationship between the two grains. An evident coincidence feature of the twins is revealed by the FFT pattern across the boundary [see Fig. 3(d)], and is determined to be $\Sigma=3$. From the image, the boundary of the twins is seen to be very sharp and lies in a definite $(1\bar{1}1)$ atomic plane.

Two possible structure models for the $\Sigma 3(1\bar{1}1)$ twin boundary are proposed in Figs. 3(e) and 3(f). The difference between the two models is that a different atomic plane (Mn–O plane or Bi–O plane) is considered to serve as the twinning plane. For each model, the twinning plane is sim-

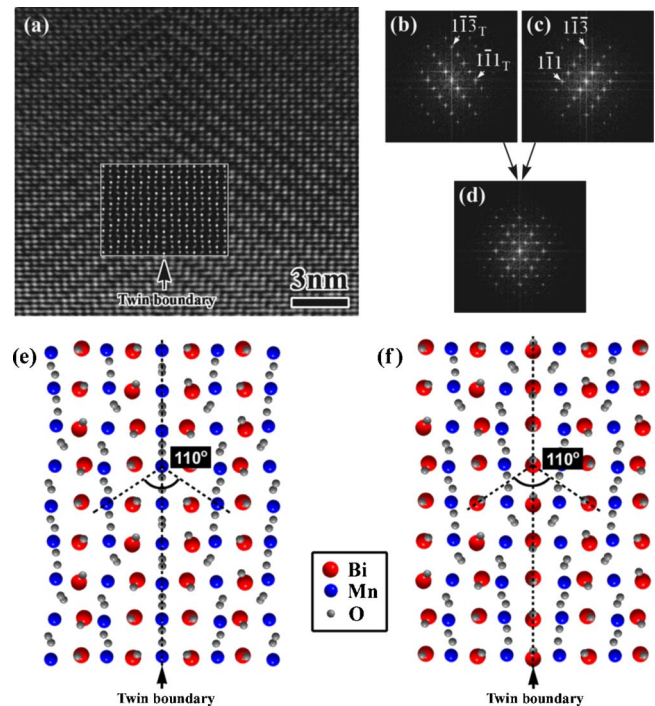


FIG. 3. (Color online) (a) HRTEM image of the $\Sigma 3(1\bar{1}1)$ twin boundary. [(b)–(d)] The FFT patterns obtained, respectively, from the left and right grains, and the region across the boundary, revealing clearly a coincidence twinning relationship between the two grains. [(e) and (f)] Two possible structure models for the $\Sigma 3(1\bar{1}1)$ twin boundary. A calculated image based on the model in (e) is superimposed onto the image in (a), appearing to be in good agreement with the experimental one.

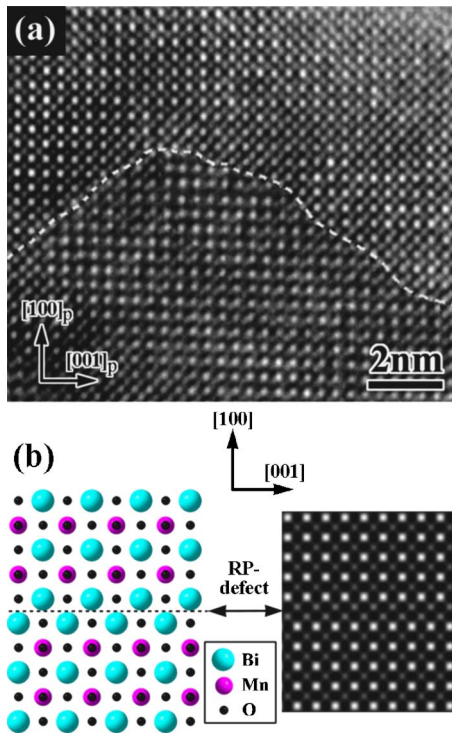


FIG. 4. (Color online) (a) HRTEM image of BiMnO_3 taken along the $[010]_p$ zone-axis direction, showing a typical RP antiphase boundary. The boundary between two RP antiphase domains is shown schematically by a dashed line. (b) The structure model of the RP planar defect on the base of an ideal cubic perovskite structure of BiMnO_3 . Beside the structural diagram is shown a calculated image of the RP defect.

plified to an exact plane by projecting those out-of-plane boundary atoms to the plane, as shown in Figs. 3(e) and 3(f). Thus the positional parameters of the atoms in the boundary plane can be derived from the known crystallographic data of BiMnO_3 , as reported in Ref. 11. To see which one of the proposed structural models is more reasonable, image simulations were carried out from them. Here we point out that the HRTEM image in Fig. 3(a) was obtained under a defocus value of ~ -63 nm. The thickness is estimated conservatively to be in the range of 10–30 nm. Considering this experimental condition, we performed the image simulations by setting the defocus value to be -63 nm and varying the crystal thickness from 10 to 30 nm. The simulated results show that a simulated image for a thickness of 17.5 nm based on the twin boundary model in Fig. 3(e), superimposed onto the image, appears to be in good agreement with the experimental one, but none of the images calculated from the one in Fig. 3(f) is found to agree with the experimental image. This indicates that the twinning plane is localized on the Mn–O atom layer. It should be noted, however, that this model is an approximate one since the positions of the atoms (especially those of the oxygen atoms) at the twinning plane cannot be determined precisely from the experiments.

In a perovskite structure, the Ruddlesden-Popper planar defect is a kind of common antiphase boundary in the $\{100\}$ planes connected with a crystallographic displacement vector of $a/2\langle 111 \rangle$.¹⁵ In our sample, we find a number of such RP antiphase boundaries. Figure 4(a) shows a HRTEM image, taken along the $[010]_p$ zone-axis direction, of a typical ex-

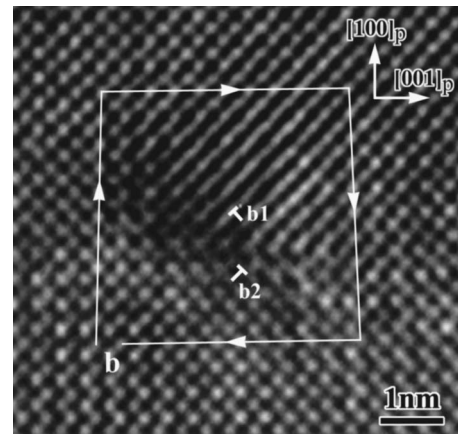


FIG. 5. HRTEM image of BiMnO_3 taken along the $[010]_p$ zone-axis direction, in which we recognize two $a_p/2\langle 111 \rangle_p$ partial dislocations b_1 and b_2 . This pair of $a_p/2\langle 111 \rangle_p$ partial dislocations constructs a typical $\langle 001 \rangle_p$ -type superdislocation.

ample of the antiphase boundaries, where the boundary between two RP antiphase domains is shown schematically by a dashed line. In general, the RP antiphase boundaries are seen to be irregular, as shown in the case of Fig. 4(a). In terms of the $C2$ monoclinic modulated superstructure, to characterize strictly the RP antiphase boundaries would be very complex and difficult. Here we give a simplified structure model on the base of an ideal cubic perovskite structure of BiMnO_3 to understand qualitatively the RP antiphase boundaries. Figure 4(b) shows the structural model of the RP planar defect viewed along the $[010]$ direction. Image simulations were carried out from this model, and a simulated image for a thickness of 17 nm and a defocus value of -73 nm is given beside the structural diagram in Fig. 4(b), where one recognizes clearly a projected displacement of $a/2[001]$ across the defect. This simulated image agrees well with the experimental one [see Fig. 4(a)], in which the projected displacement of $a_p/2[001]_p$ across the boundary is also clearly visible [see Fig. 4(a)]. Generally, dislocations are formed at the ends of a RP antiphase boundary if the boundary stops within a crystal and their Burgers vector usually equals the displacement vector of the antiphase boundary.

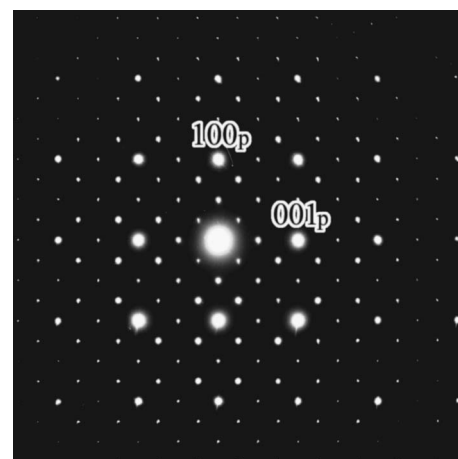


FIG. 6. ED pattern taken along the $[010]_p$ zone-axis direction of the irradiation-induced $4a_p \times 4b_p \times 4c_p$ modulated structure.

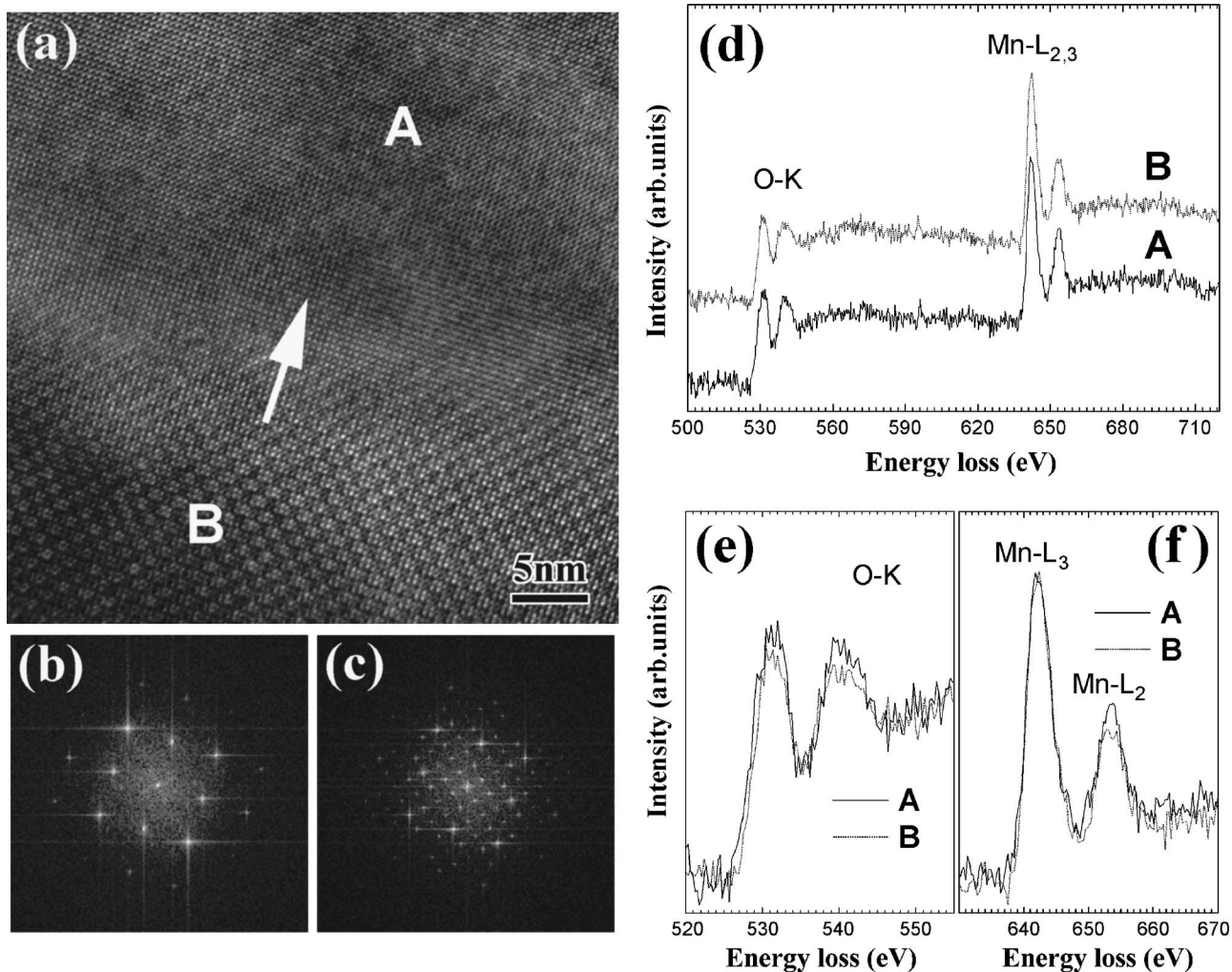


FIG. 7. (a) HRTEM image of BiMnO₃ taken along the [010]_p zone-axis direction, showing that the $4a_p \times 4b_p \times 4c_p$ modulated phase (domain B) coexists with the C2 monoclinic form (domain A). [(b) and (c)] The FFT patterns corresponding to the domains A and B in (a), respectively. (d) EELS spectra obtained from the domains A and B in (a). (e) Enlargement of O-K edges. (f) Enlargement of Mn-L_{2,3} edges.

The dislocations together with the ribbon of antiphase boundary between them construct a superdislocation.¹⁶

In most cases, superdislocations associated with a small segment of RP defect are formed in the perovskite structure. Based on geometrical considerations, four types of superdislocation with different arrangements of the $a/2\langle 111 \rangle$ partials can be derived as $\langle 110 \rangle$, $\langle 001 \rangle$, $\langle 111 \rangle$, and null types.¹⁷ In our BiMnO₃ sample, we observed a number of $\langle 001 \rangle$ -type superdislocations. Figure 5 shows a HRTEM image taken along the [010]_p zone-axis direction, in which we first recognize two $a_p/2\langle 111 \rangle_p$ partial dislocations, b_1 and b_2 . The projections of the Burgers vectors of the two partials are $a_p/2[101]_p$ and $a_p/2[\bar{1}01]_p$, respectively. The projected sum of the two partial dislocations is $b_{\text{proj}} = a_p/2[101]_p + a_p/2[\bar{1}01]_p = a_p[001]_p$, as shown clearly by a large Burgers circuit around the whole defect region. Considering their arrangements at the end of the RP defect, this pair of $a_p/2\langle 111 \rangle_p$ partial dislocations constructs a typical $\langle 001 \rangle_p$ -type superdislocation. In addition, we would point out that no single $a_p/2\langle 111 \rangle_p$ partial dislocation formed by inserting a small segment of RP defect is visible in our sample.

C. Electron-irradiation-induced voids (ordered oxygen vacancies)

With the process of our TEM work, another commensurate modulated superstructure was gradually visible in the sample. Figure 6 shows an ED pattern of this kind of modulated phase taken along the [010]_p zone-axis direction. This modulated phase displays an apparently higher symmetry (pseudocubic) and can be characterized as a body-centered pseudocubic superstructure with the lattice constants of $4a_p \times 4b_p \times 4c_p$ (where, in fact, the three axes a_p , b_p , and c_p of the fundamental perovskite substructure cannot be differentiated strictly from one another by ED). The $4a_p \times 4b_p \times 4c_p$ modulated phase was also observed by Montanari *et al.*¹⁸ and Chiba *et al.*¹⁹ in their high-pressure BiMnO₃ samples, and was explained to be an intrinsic polymorph of BiMnO₃ formed under high temperature and high pressure. It is interesting, however, that in our sample this $4a_p \times 4b_p \times 4c_p$ modulated phase was found to develop just from the C2 monoclinic form during our TEM observations and was not present initially. More detailed characteristics and evolutions of this form will be reported elsewhere.

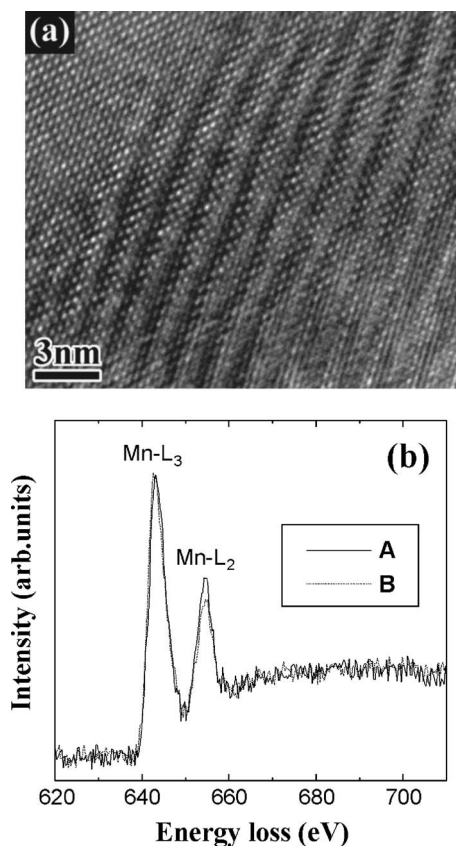


FIG. 8. (a) HRTEM image of another modulated structure (completely different from the $4a_p \times 4b_p \times 4c_p$ one) developed from an area after continuous irradiation for 15 min under the electron beam. (b) Mn- $L_{2,3}$ absorption edges obtained from the irradiation-induced modulated structure (curve B) and the same area before its formation (curve A).

We note that the transition to the $4a_p \times 4b_p \times 4c_p$ modulated structure is not simultaneous for all the grains; even for a single grain the transition occurs also nonsimultaneously in different regions. This is why we sometimes observe the $4a_p \times 4b_p \times 4c_p$ modulated form coexisting with the $C2$ monoclinic form. As an example, Fig. 7(a) shows a HRTEM image of a coexisting region of the two forms, where the domains A and B refer, respectively, to the latter and the former ones, as suggested by their corresponding fast Fourier transforms given, respectively, in Figs. 7(b) and 7(c). When these coexisting regions are continuously exposed to the electron beam, the $4a_p \times 4b_p \times 4c_p$ modulated phase is clearly observed to extend gradually at the expense of the $C2$ monoclinic phase. In Fig. 7(a), the white arrow shows the advancing direction of the $4a_p \times 4b_p \times 4c_p$ phase (domain A). In order to see whether chemical effects result in the irradiation-induced form, an attempt was made to compare its composition with that of the $C2$ monoclinic form. Figure 7(d) shows the EELS spectra obtained from domains A (spectrum A) and B (spectrum B) in Fig. 7(a), and each spectrum includes the O-K and Mn- $L_{2,3}$ absorption edges. The enlarged O-K and Mn- $L_{2,3}$ edges are shown in Figs. 7(e) and 7(f), respectively. To obtain the enlarged O-K edges, we normalize the two spectra in Fig. 7(d) to have the same Mn- $L_{2,3}$ integrated counts. The enlarged O-K edges show clearly that the O-K edge obtained from the $4a_p \times 4b_p \times 4c_p$ modulated form (domain B) is lower than that ob-

tained from the $C2$ monoclinic form (domain A), indicating that some oxygens are lost in the former. This result is reinforced by comparing the Mn- $L_{2,3}$ edges obtained from the two forms. From Fig. 7(f) one can see that the L_3/L_2 intensity ratio for the $4a_p \times 4b_p \times 4c_p$ form is slightly higher than that for the $C2$ monoclinic form, indicating that the manganese in the former shows a lower valence state according to the well known relationship between the L_3/L_2 intensity ratio and the valence state for Mn ions.²⁰ Since no additional cations (Bi and Mn) are introduced into the grain during the irradiation, the unique interpretation for the decrease of Mn valence state is that some oxygens are lost. The EELS results suggest that the irradiation-induced $4a_p \times 4b_p \times 4c_p$ modulated phase originates clearly from an ordered oxygen deficiency.

Occasionally, some other ordered oxygen-deficient modulated structures are also observed to be produced by the electron-beam irradiation. As an example, Fig. 8(a) shows a HRTEM image of another modulated structure (completely different from the $4a_p \times 4b_p \times 4c_p$ one mentioned above) developed from an area after continuous irradiation for 15 min under the electron beam. Mn- $L_{2,3}$ absorption edges from the irradiation-induced modulated form and the same area before its formation were measured and shown in Fig. 8(b) by curves B and A, respectively. The Mn- $L_{2,3}$ EELS results show clearly that the Mn ion valence state is lower in the irradiation-induced modulated form than in its initial $C2$ monoclinic form, indicating that (ordered) oxygen vacancies are also introduced into this modulated form by electron-beam irradiation.

Finally, we would point out that the magnetic measurements on our BiMnO₃ sample reveal, as expected, a typical ferromagnetic transition (Ref. 14) which agrees with most of the reported results.³⁻⁷ No evidence from the magnetic investigations indicates that the sample is of polyphasic nature, as reported in Ref. 18. The ferromagnetic results could exclude the possibility of the presence of other BiMnO₃ polymorphs in our as-synthesized sample, which agrees with the TEM results; i.e., all the ordered oxygen-deficient modulated structures, such as the $4a_p \times 4b_p \times 4c_p$ one, are developed just from the $C2$ monoclinic form under the electron-beam irradiation and are not present initially. The exact influences of the irradiation-induced ordered oxygen vacancies on the magnetoferroelectricity for the multiferroic BiMnO₃ will be confirmed by studying a bulk sample which suffered from electron irradiation. This work is under way.

IV. CONCLUSIONS

In this paper, we reveal in the high-pressure synthesized multiferroic material BiMnO₃ some important structural defects at atomic scale by means of TEM and EELS. $\Sigma 3(1\bar{1}1)$ twin boundaries, RP antiphase boundaries, and superdislocations associated with a small segment of RP defect are frequently visible in the sample. High-resolution TEM study, in combination with theoretical simulation, demonstrates that the twinning plane of the $\Sigma 3(1\bar{1}1)$ twin boundary is localized on a Mn-O atom layer. The superdislocations composed of a pair of $a_p/2\langle 111 \rangle_p$ partial dislocations are seen generally to

be equivalent to a perfect dislocation with Burgers vector of $a_p\langle 001 \rangle_p$. These defects are present initially in the sample, unlike the products induced by electron-beam irradiation. In addition, ordered oxygen vacancies are found to be easily introduced into the multiferroic BiMnO_3 by electron-beam irradiation. During our TEM observation, some other modulated phases such as the $4a_p \times 4b_p \times 4c_p$ body-centered pseudocubic one are found to develop from the initial C2 monoclinic form due to the electron-beam irradiation. The O-K and Mn- $L_{2,3}$ EELS results suggest that these irradiation-induced modulated phases are oxygen deficient.

ACKNOWLEDGMENTS

This work was supported by the National Natural Science Foundation of China (Grant Nos. 50471053, 50321101, 50332020, and 90401003) and the State Key Development Program for Basic Research of China (Grant Nos. 2005CB623602 and 2002CB613301).

¹N. A. Hill and K. M. Rabe, Phys. Rev. B **59**, 8759 (1999).

²A. N. Hill, J. Phys. Chem. B **104**, 6694 (2000).

³F. Sugawara, S. Iida, Y. Syono, and S. Akimoto, J. Phys. Soc. Jpn. **20**, 1529 (1965).

⁴A. F. Moreira dos Santos, A. K. Cheetham, W. Tian, X. Q. Pan, Y. F. Jia,

N. J. Murphy, J. Lettieri, and D. G. Schlomb, Appl. Phys. Lett. **84**, 91 (2004).

⁵A. Moreira dos Santos, S. Parashar, A. R. Raju, Y. S. Zhao, A. K. Cheetham, and C. N. R. Rao, Solid State Commun. **122**, 49 (2002).

⁶E. Ohshima, Y. Saya, M. Nantoh, and M. Kawai, Solid State Commun. **116**, 73 (2000).

⁷H. Faqir, H. Chiba, M. Kikuchi, Y. Syono, M. Mansori, P. Satre, and A. Sebaoun, J. Solid State Chem. **142**, 113 (1999).

⁸R. Seshadri and N. A. Hill, Chem. Mater. **13**, 2892 (2001).

⁹N. A. Hill and K. M. Rabe, Phys. Rev. B **59**, 8759 (1999).

¹⁰T. Kimura, S. Kawamoto, I. Yamada, M. Azuma, M. Takano, and Y. Tokura, Phys. Rev. B **67**, 180401(R) (2003).

¹¹T. Atou, H. Chiba, K. Ohoyama, Y. Yamaguchi, and Y. Syono, J. Solid State Chem. **145**, 639 (1999).

¹²D. Bolten, U. Böttger, and R. Waser, Jpn. J. Appl. Phys., Part 1 **41**, 7202 (2002).

¹³Q. Tan, J. X. Li, and D. Viehland, Appl. Phys. Lett. **75**, 418 (1999).

¹⁴Z. H. Chi, C. J. Xiao, S. M. Feng, F. Y. Li, C. Q. Jin, X. H. Wang, R. Z. Chen, and L. T. Li, J. Appl. Phys. **98**, 103519 (2005).

¹⁵S. N. Ruddlesden and P. Popper, Acta Crystallogr. **11**, 54 (1958).

¹⁶S. Amelinckx, in *Dislocations in Solid*, edited by F. R. N. Nabarro (North-Holland, Amsterdam, 1979), Vol. 2.

¹⁷J. S. Wu, C. L. Jia, K. Urban, J. H. Hao, and X. X. Xi, J. Cryst. Growth **234**, 603 (2002).

¹⁸E. Montanari, L. Righi, G. Calestani, A. Migliori, E. Gilioli, and F. Bolzoni, Chem. Mater. **17**, 1765 (2005).

¹⁹H. Chiba, T. Atou, H. Faqir, M. Kikuchi, Y. Syono, Y. Murakami, and D. Shindo, Solid State Ionics **108**, 193 (1998).

²⁰Z. L. Wang, J. S. Yin, and Y. D. Jiang, Micron **31**, 571 (2000).